Pressure-velocity correlations in a shock wave boundary layer interaction

Tetyana Jiang

Centre National d Études Spatiales
CNES, DLA
75612 Paris Cedex, France
tetyana.jiang@univ-amu.fr

Sébastien Piponniau

Aix Marseille Univ
CNRS, IUSTI
13453 Marseille cedex 13, France
sebastien.piponniau@univ-amu.fr

Pierre Dupont

Aix Marseille Univ
CNRS, IUSTI
13453 Marseille cedex 13, France
pierre.dupont@univ-amu.fr

ABSTRACT

We present here experimental results in a shock wave / turbulent boundary layer interaction at Mach number of 2, impinged by an oblique shock wave, with a deflection angle of 8°, as installed in the supersonic wind tunnel of the IUSTI laboratory, France. This kind of interaction is characterised by strong unsteadiness, both at low and medium frequency compared to the energetic scales of the incoming boundary layer. The paper deals with simultaneous dual-PIV velocity fields and unsteady wall pressure measurements. The wall pressure and dual-PIV measurements were used to characterize the pressure distribution at the wall in an axial direction, and the flow field associated.

POD decomposition of the flow has been applied to dual-PIV measurement, using a single projection basis. Thanks to the dual-PIV possibilities, integral time scales of the different POD modes have been computed. Pressure-velocity correlation is then discussed in this paper, combining a frequency filtering of the pressure signal, and a POD modes selection based on their integral scales. First results are presented here and show the success of this method, by strengthening the correlation at low or medium frequency. These results are planned to be used in the future as an input for Linear Stochastic Estimation, where the quality of this kind of correlation is of major importance for better estimation of the flow field.

Introduction

Shock waves / boundary layer interactions are complex phenomena occurring in various aeronautical configurations, such as over-expanded nozzles or air intake. When the shock is strong enough to make the boundary layer separate, a strong unsteadiness is observed, with typical frequencies at least two order of magnitude lower than the energetical frequencies of the incoming boundary layer. These interactions lead to important aerodynamic and thermal loads which can be harmful for the structure. Both the separation shock wave and the recirculating bubble are subjected to low frequency unsteadiness (Dolling (2001); Ganapathisubramani *et al.* (2009); Wu & Martin (2008) among others). However, recent work suggested that this low frequency unsteadiness could be related to the mass entrainment due to the development of a mixing layer on the boundary of the recirculating bubble, but occurring at a frequency an order of magnitude higher than the characteristic low frequency (Piponniau *et al.* (2009)). Understanding the mechanisms leading to low frequency unsteadiness is thus quite challenging, and needs a better comprehension of the spatio-temporal dynamic of the turbulent structures of the mixing layer.

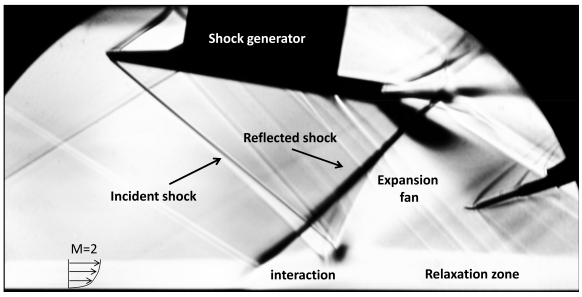

Figure 1. Schlieren visualisation of the flow

The present study deals with simultaneous measurements of unsteady wall pressure and Dual-PIV measurements in a shock wave / boundary layer interaction at Mach number 2 with a deflection angle of 8.5° (Schreyer *et al.* (2015*b*)). Velocity information is exploited using a POD decomposition. Thanks to the Dual-PIV database, it has been possible to compute the integral time scale of the different POD modes, and to select these modes according to their frequency signature. These modes are then used for pressure/ velocity correlation, to provide a more detailed information of the spatio-temporal behaviour of the interaction. Using this method, the low frequency correlation is reinforced using this method, and, while a classical pressure /velocity correlation doesn't exhibit significant correlation at medium frequency, it is here possible to extract features located in the mixing layer development, with an associated convective scheme.

1 Experimental Set Up

Experiments are carried out in the hypo-turbulent supersonic wind tunnel of the IUSTI laboratory, at the Aix-Marseille University, France. This is a continuous facility with a closed-loop circuit. The nominal Mach number of the test section is $M = 2$. The incident shock wave is generated by a sharped leading edge fixed on the ceiling of the test section, with an inclination θ, fixed here at $\theta = 8.5°$. For such flow deviations, the flow has been controled to separate. The incoming conditions of the interaction are summarized in Tab. 1 and a Schlieren visualisation of the flow is presented Figure 1.

The rectangular test section is 170*mm* wide by 105*mm* height. The origin of the longitudinal coordinate X was fixed at the mean

Table 1. Flow parameters

M_∞	p_0	T_0	Re_θ	θ	L
2.0	40500 Pa	295 K	4850	8.5°	58 mm

position X_0 of the unsteady reflected shock on the axis of the wind tunnel. This position was derived from Schlieren visualisation and longitudinal Hot wire measurements. Coordinates are normalized by the length of the interaction L, defined as the distance between the mean position of the reflected shock and the extrapolation down to the wall of the incident shock: the interaction extends from $X^* = 0$ to $X^* = 1$.

1.1 Dual PIV measurements

Basically, Dual-PIV systems consists of two independent PIV systems, observing exactly the same field of view. These two systems are controlled by a "Fast Digital Controller to obtain an adjustable delay $\delta\tau$ between the two acquisitions : $0 \leq \delta\tau \leq \infty$. If recent time-resolved PIV systems can attain temporal resolutions of up to O(50 kHz) (Beresh *et al.* (2015)) and even larger frequency if supersampling algorithm are used Scarano & Moore (2012); Beresh *et al.* (2016), this high temporal resolution is at the expense of the spatial resolution. On the contrary, dual PIV measurements allow the determination of spectral informations of up to O(100 kHz), together with a high spatial resolution as for classical PIV systems (Schreyer *et al.* (2015*a*); Jiang *et al.* (2016)).
The Dual PIV system used for these experiments is based on the frequency separation of the two systems : two lasers of different wavelengths, 537nm and 532nm, illuminate the same field of view. The lasers deliver respectively 200mJ and 180mJ per pulse. Image separation is achieved with optical color filters, one low-pass and one narrow band-pass filter, in front of the camera lenses.

Two high-resolution Hisense 630 (PCO 4000, 4008×2672 pixels) cameras with an interframe delay of $1\mu s$ and equipped with Zeiss 100mm, $f:2$ objectives are used. The high-sensitivity, 11 MPixel, CCD sensor of large dimension (24×36 mm) results in large pixel size and high electronic sensitivity. Incense smoke is used as seeding particles. Particles are injected from the wall, upstream of the sonic section of the wind tunnel, and are naturally entrained into the flow since the total pressure of the flow is less than the atmospheric pressure. The diameter of the particle is estimated to be of $0.5\mu m$, with a frequency response of about 200kHz (Piponniau *et al.* (2009). For more details about the Dual PIV setup, a full description of the system can be found in Schreyer *et al.* (2015*b*).

In order to describe accurately the wide range of time scales expected in such flow, dual PIV measurements has been used for the acquisition of 24 time delays between the two cameras ranging from $0\mu s$ to $3000\mu s$. The time grid for the delay time was adjusted as in Tab. 2. The set with $0\mu s$ delay time, simultaneous measurements, is used to quantify the noise of the dual-PIV system as well as the decomposition on a unique base of the different data-sets (see next section). For each time delay, 2500 instantaneous PIV vector fields were acquired for both cameras. This leads to a database of 60,000 instantaneous PIV vector fields.

1.2 Pressure measurements

Simultaneously with dual-PIV measurements, unsteady pressure measurement are acquired along the interaction region, in the exact location of PIV measurements, on the axis of the wind tunnel.

Table 2. Definition of the discretization of the time delays $\tau_i[\mu s]$ available from the Dual–PIV measurements.

$0 \rightarrow 20$	$40 \rightarrow 100$	$140 \rightarrow 500$	$1000 \rightarrow 3000$
5	20	40	500

We used *kulite XCQ-062* miniature pressure sensors, placed behind a cavity to avoid incense clogging of the thin and fragile membrane of this kind of sensors. The cavity is of the same type as in Piponniau *et al.* (2012), and it has been shown that there is no significant dumping or phase shift up to $10KHz$.
Seven Kulite sensors were used for these experiments, one is placed upstream of the interaction region, in the upstream turbulent boundary layer, and the other 6 are placed longitudinally along the interaction. After amplification in a *Karl Tesar D582* differential amplifier, pressure signals are acquired using a *NI-PXI 6133* acquisition card, at a sampling frequency of $200KHz$. The acquisition start on the camera trigger of the camera #1, and 8192 time steps are acquired centered around the trigger.

2 Proper orthogonal Decompostion

2.1 Reminders

A proper orthogonal decomposition (POD) is performed on the set of 2 500 instantaneous PIV vector fields of the first camera $C1$, and for the dual-PIV time delay $\delta\tau = 0$. The POD consists in extracting the spatial structure $\Phi(\mathbf{x})$ from the flow, with the largest mean-square projection onto the velocity field $\mathbf{u}(\mathbf{x},t)$. The maximization problem leads to the solving of the integral problem of eigen values:

$$\int_{\mathscr{D}} R(\mathbf{x},\mathbf{x}')\ \Phi_n(\mathbf{x}')d\mathbf{x}' = \lambda_n\ \Phi_n(\mathbf{x}) \tag{1}$$

where λ_n corresponds to the n^{th} eigen value and represents the amount of energy contained in the spatial mode $\Phi_n(\mathbf{x})$. $R(\mathbf{x},\mathbf{x}')$ is the two-point temporal correlation tensor defined as $R(\mathbf{x},\mathbf{x}') = \langle \mathbf{u}(\mathbf{x},t)\mathbf{u}(\mathbf{x}',t)\rangle$, where $\langle\cdot\rangle$ is the ensemble average operator. The modes are sorted in the descending order: $\lambda_1 > \lambda_2 > \cdots > \lambda_{N_{POD}} > 0$.

In the context of the present study, we use a snapshot POD method (Sirovich, 1987) to extract POD modes from the PIV dataset. The fluctuating field can be projected onto the POD orthonormal basis, composed of the eigen functions $\Phi_n(\mathbf{x})$:

$$\mathbf{u}(\mathbf{x},t) = \sum_{n=1}^{N_{POD}} a_n(t)\cdot\Phi_n(\mathbf{x}) \tag{2}$$

where N_{POD} is here the number of PIV samples. The variancy of the temporal projection coefficients $a_n(t)$ corresponds to the energy described by the mode n:

$$\langle a_i \cdot a_j\rangle = \delta_{ij}\,\lambda_i \tag{3}$$

2.2 POD applied to DUAL PIV measurements

Specificities of the dual PIV is to have acquisition of PIV vector fields from 2 distinct cameras, looking at exactly the same field of view. It could be possible to perform a POD decomposition for each set of data coming from both cameras, but in this case two different bases can be expected. Nevertheless, as same fields of view

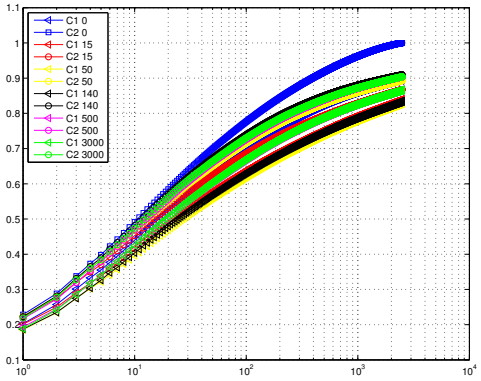

Figure 2. cumulative relative energy

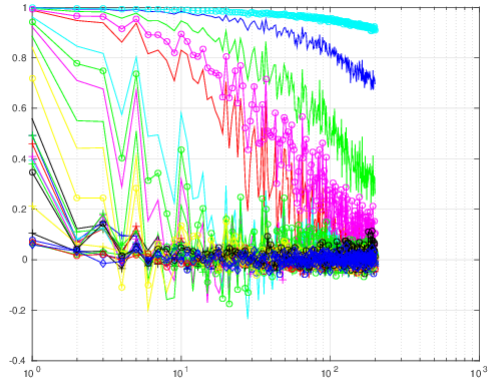

Figure 3. Intercorrelation functions for the different modes for various delay times (0 to 3000μs)

are analyzed, one could think that, if a POD analysis is made on one set of data, the spatial modes $\Phi_n(\mathbf{x})$ should be adapted to the second one, even for non null time delay $\delta\tau$. The idea is here to select a projection basis $\Phi_n^0(\mathbf{x})$, and then making the POD decomposition of the flow, from all the acquisitions, using this unique basis.
The end result can be put in a matrix form to find the temporal coefficients of each acquisition sequence :

$$a_n(t+\delta\tau) = [u_{\delta\tau}]^t \cdot [\Phi_n^0(x)] \tag{4}$$

where the notation $\delta\tau$ refers to the considered dual PIV acquisition, $a_n(t+\delta\tau)$ are the calculated temporal coefficients of the acquisition, $[u_{\delta\tau}]$ is the matrix containing the velocity informations, and $[\Phi_n^0(x)]$ the matrix of the spatial modes retained for unique POD decomposition. For better readability, no difference between the two cameras is made in the last equation. Applying this procedure to all the Dual PIV acquisitions leads to have a database, with a common spatial mode decomposition, and a set of temporal modes for each acquisition. POD decomposition is applied here using the whole set of spatial modes, meaning $N_{modes} = N_{PIV} = 2500$ snapshots in our configuration. The simultaneous dual-PIV data set ($\delta\tau = 0$) was used to build the reference base.
A first verification of the projected temporal modes is made by evaluating the energy spectrum compared to the original decomposition. The temporal projection coefficients $a_n(t+\delta\tau)$ contains the energy:

$$< a_i(t) \cdot a_j(t+\delta\tau) >= \delta_{ij}\lambda_i \tag{5}$$

Figure 2 represents the cumulative energy of the original decomposition ($C1\ 0$ curve) and the cumulative energy of the PIV vector fields, for the other acquisitions as well as for each cameras. Naturally, the cumulative energy of the original POD decomposition ($C1\ 0$: camera 1 , $dt = 0$) is at 100 % using all the modes and is the most efficient to rebuild the total energy. The decomposition of the camera 2, for the same time delay of 0μs, meaning that the two PIV snapshots coming from each camera are taken exactly at the same time, is presented on the $C2\ 0$ curve : the percentage of energy reconstructed is of about 90% of the original decomposition. Figure 2 shows that, despite the base derived from the first camera data set is not optimal, it is efficient to rebuild the energy of the velocity field. Looking at the other decompositions, for several time delays between the two cameras of 15μs to 3000μs, we see that the energy differs from the original decomposition in a similar way than when the second camera with zero delay time is considered. For the worst cases the energy contained in the temporal projection is of 80% of the reference case. It is worth to mention that several experiments, for different wind tunnel start up, are considered. This shows that the experiments are highly repeatable. Moreover, as described in next sections, the modes being considered for further analysis are the first 100 modes. Therefore, we can considered that the decomposition for these modes range is efficient from an energetic point of view.

3 Time properties of the temporal coefficients

Once the temporal coefficient for each $\delta\tau$ experiments are obtained, it is then possible to evaluate a characteristic time scale for each modes. It has been derived from the intercorrelation coefficient $I_i(\tau)$:

$$I_i(\delta\tau) = \frac{< a_i(t) \cdot a_i(t+\delta\tau) >}{\sigma_{a_i(t)}\sigma_{a_i(t+\delta\tau)}} \tag{6}$$

where $I_i(\delta\tau)$ is the intercorrelation coefficient at a time delay $\delta\tau$ for the mode i, $\sigma_{a_i(t)}$ and $\sigma_{a_i(t+\delta\tau)}$ the RMS of the temporal modes, and the parameter $t+\tau$ is the time delay between the two cameras of the dual PIV. $\sigma_{a_i(t)}$ and $\sigma_{a_i(t+\delta\tau)}$ can be slightly different are they are derived respectively from the two different set of data given by the dual PIV.

The autocorrelation $I_i(\delta\tau)$ is reported Figure 3 as a function of the mode i for different delay times. It is clear from this figure that the different modes are involving very different range of time scales. Moreover, the energetic classification from the POD is found to follow qualitatively the classification in time: when higher mode are considered, they describe less and less energy and smaller time of correlation are observed. The autocorrelation $I_i(\delta\tau = 0)$ is reported in cyan on the figure. If there was no noise from the dual-PIV system (a correlation of one between the two unsteady velocity fields derived from both PIV systems) as well as from the projection of the second field on a non optimal base, we should obtain a correlation coefficient of one for all the modes. It is clear that for the first two hundred modes, very high correlation coefficients are obtained ($I_i(\delta\tau = 0) > 0.9$). These modes represent more than 85% of the total energy: this indicate that very limited noise is coming from the dual-PIV measurements and from the projection.
To quantify the time of correlation for each mode, the integral time scale $\mathscr{T}$ of the temporal coefficient of the mode i is defined as:

$$\mathscr{T} = \int I_i(\delta\tau) d\tau \tag{7}$$

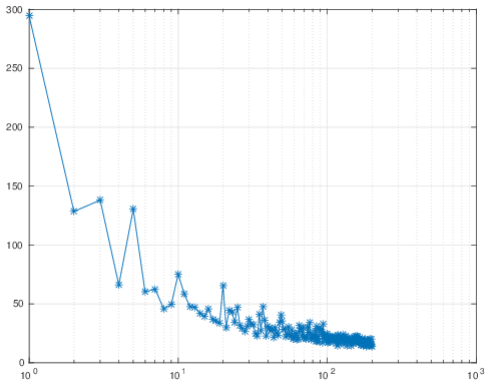

Figure 4. Integral time scales for the different modes

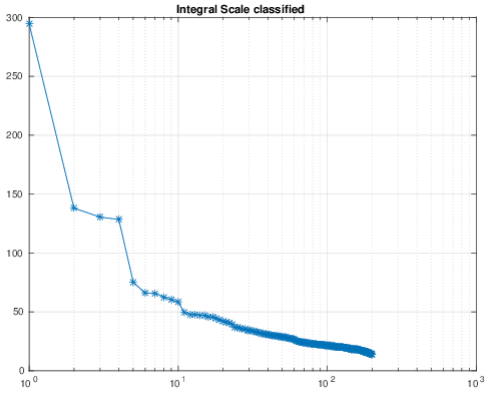

Figure 5. Re-ordered Integral time scales for the different modes

As the time delays discretization increases dramatically for $\delta\tau \geq 500\mu s$, the integral is estimated only for $0 \leq \delta\tau < 500\mu s$ in order to avoid spurious integration values. This corresponds at least 10 times the expected integral scale of the turbulent velocity fluctuations in the upstream turbulent boundary layer.

Figure 4 represents the integral scale for the first 200 POD modes. As expected, the main decrease of the integral time scale with the order of the mode is observed. But we also see that all the modes are not totally in order from the largest integral scale to the smallest. The modes have been then reordered by their integral scale, as shown on Figure 5.
From the figure, different characteristic set of modes can be identified:

the first mode, involving very large time scale ($\mathscr{T} \simeq 600\mu s$)
the modes $2 \rightarrow 4$ with slightly smaller time scales ($\mathscr{T} \simeq 125\mu s$)
the modes $5 \rightarrow 10$with time scales remaining over $50\mu s$
the modes > 10, with continuously decreasing time scales.

It is quite obvious to associate the two first family with the very low frequency motions of the interaction. The other sets are more difficult to characterize. In order to associate these modes with the low and medium frequencies pressure fluctuations, simultaneous pressure and dual-PIV measurements are used.

4 Optimization of pressure velocity correlation using POD decomposition

The objective is to use the POD decomposition as a filter for pressure-velocity correlation, especially to separate low and

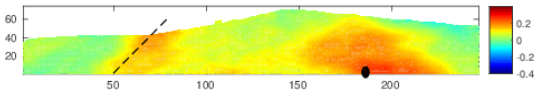

(a) Original velocity field

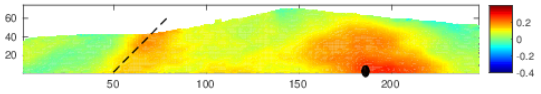

(b) 100 POD modes reconstructed velocity field

Figure 6. Pressure- velocity correlation

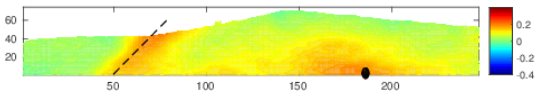

(a) Original velocity field

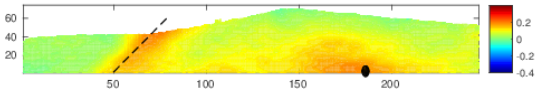

(b) 100 POD modes reconstructed velocity field

Figure 7. low frequency filtered Pressure and raw velocity correlation

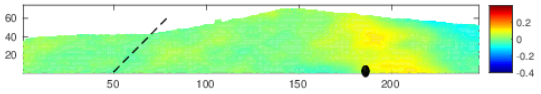

(a) Original velocity field

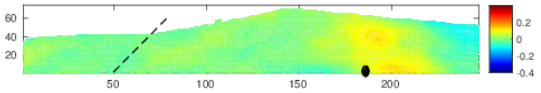

(b) 100 POD modes reconstructed velocity field

Figure 8. medium frequency filtered Pressure and velocity correlation, at a $\delta\tau = 0\mu s$

medium frequency unsteadiness. Pressure measurements are made using kulite type pressure sensors: as mentioned previously, these sensors have a frequency response of less than $20KHz$, meaning a characteristic response time of $50\mu s$: we see that modes higher than mode 100 should be of no interest in the context of the paper, since mode 100 has a characteristic time of about $20\mu s$.
Figure 6(a) shows the pressure-velocity correlation for the pressure sensor 5 using the original PIV vector field, and the same correlation but using 100 modes for velocity reconstruction is reported Figure 6(b): the energy represented by the first 100 modes is of about 80% of the original energy (see figure 2). On each correlation map, the mean position of the unsteady separation shock wave is represented using dashed dots and the position of the considered pressure sensor is marked with a black point. Apart from a slight smoothing due to the data reduction of the POD decomposition, we see that both correlation map have the same aspect. This shows that a 100 modes decomposition of the PIV vector field is enough to capture most of the important features of the velocity-pressure correlation field.

The results obtained from the integral time scale of the tempo-

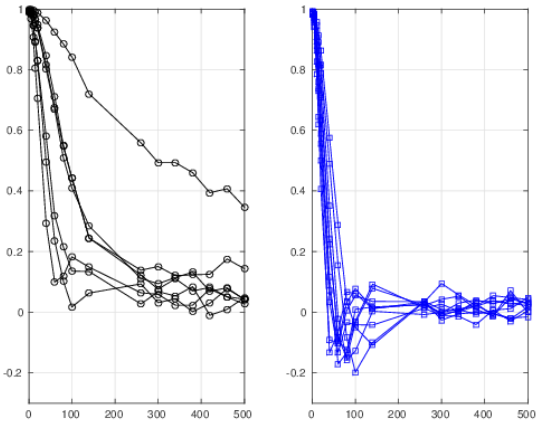

Figure 9. Autocorrelation functions of the temporal coefficents for different modes

ral coefficient have been used to optimized the pressure velocity correlation. The pressure signals were filtered using two different bandwidth frequency. A low pass filter with a cut-off frequency of $1KHz$, was used in order to exhibits the low frequency features of the flow : the characteristic frequency of the separation shock is of $300Hz$, as well as the the low frequency breathing of the separation bubble (Dupont *et al.* (2006)). A band-pass filter with a bandwidth frequency of $1-20KHz$ was used to exhibits the medium frequency parts of the flow, typically the shear layer and the relaxation of the flow.

Figure 7 show the results of the correlation after having low passed the pressure signal. We see that correlation is slightly changed: this shows that the broadband pressure-velocity correlation is dominated by the low frequency motions of the interaction. Again, a reconstruction of the velocity field based on 100 modes give equivalent results.

Figure 8 shows results for the medium frequencies. In this case, the separation shock region disappear as expected. Only the downstream region exhibits significant pressure-velocity correlations. Again, using 100 modes POD decomposition or the original field does not lead to significant differences.

As discussed in the previous section, integral scale of each POD modes has been reordered from the largest to the smallest integral scales. Only modes with integral scales larger than $40\mu s$ have been considered (modes 1 to 32, see figure 5). The analysis of the integral scale was efficient to separate several low frequency modes ($1 \rightarrow 9$). Nevertheless, it is quite difficult, based only on this parameter, to classify the remaining modes. Therefore, the autocorrelation functions for these range of modes have been considered. They are reported Figure 9. Two different sets have been observed. On the left figure, classical autocorrelation coefficients, continuously decreasing, are obtained, with rather large integral scales. On the right figure, several mode exhibit temporal coefficients with oscillating autocorrelation functions. Therefore, two sets of modes have been defined: the first one corresponding to the mode $1 \rightarrow 9$ associated with low frequency motions and the second one, corresponding to the oscillating autocorrelation functions as shown Figure 9.

Figure 10 show the pressure-velocity correlation map for the low-pass filtered pressure fluctuations and the first set of modes. Two different pressure sensors are shown: their positions are reported on the figure with a black point. The Figure 10(a) has to be compared to Figure 7: we see that correlation is strengthened. The separation shock wave and the recirculating bubble are well correlated.

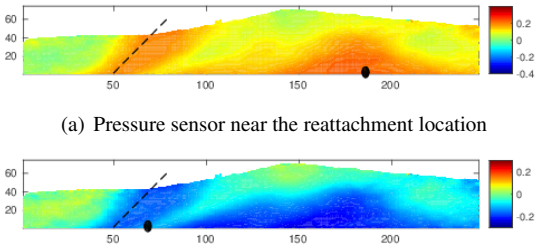

(a) Pressure sensor near the reattachment location

(b) Pressure sensor near the separation location

Figure 10. Pressure-velocity correlation, using low passed pressure signal and selected modes.

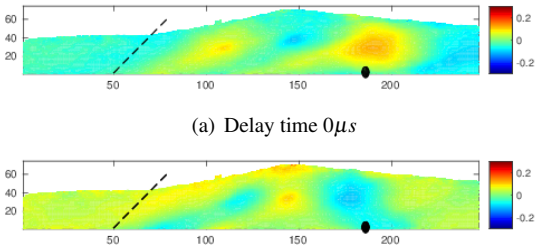

(a) Delay time $0\mu s$

(b) Delay time $125\mu s$

Figure 11. Correlation for band passed pressure signal and selected modes

When the pressure sensor is located in the vicinity of the separation point, see Figure 10(b), an equivalent anti-correlated field is observed. This was expected: contractions of the separated region are associated with a decrease of the pressure near the separation (the separation shock moves downstream) and an increase of the velocity near the wall. This confirms a global low frequency motion of the interaction. The results shown Figure 10(a), with the pressure sensor near the reattachment location, suggest an in-phase variations of the velocity and pressure low-frequency fluctuations. This suggests an increase of the pressure when the bubble is contracting. This is coherent with results reported in Agostini *et al.* (2015). From LES computations, low frequency breathings of the separation bubble were analyzed. Large contractions, respectively dilatations, of the bubble were observed, associated with an increase, respectively decrease, of the pressure.

For the medium frequency correlation map, the POD filtering changes dramatically the pressure-velocity correlation map, see Figure 11. The pressure-velocity correlation levels are significantly increased in the shear layer region and a periodic pattern in space is observed. Two different maps are reported: Figure 11(a) corresponds to a null time delay between the band-passed pressure and velocity fluctuations and Figure 11(a) corresponds to a time delay of $125\mu s$ between both signals. This suggest convective motions of large scales along the separated shear layer.

5 Conclusion

The low and medium frequency unsteadiness which are developing in a separated Shock Wave Boundary Layer Interaction are investigated with synchronized dual-PIV and unsteady wall pressure measurements. Several velocity fields, with a wide range of time delays, are acquired. Their decompositions on a unique base, derived from the Proper orthogonal Decomposition of one of the data set, allow to evaluate the autocorrelation function of the tem-

poral coefficient associated to the spatial modes of the base. From the time properties of these autocorrelation functions, it is possible to identify two subset of modes contributing respectively to the low and medium frequency unsteadiness of the interaction. As expected, low frequencies involve the whole interaction which is strongly correlated with the low frequency separation shock motions. We confirm previous results derived from Large Eddy Simulations: the shrinking of the separation bubble correspond to an increase of the pressure with an opposite trend for its swelling. Medium frequencies seem associated with large convective structures, shed downstream from the reattachment. This new analysis is a first attempt to apply spatio-temporal filters on instantaneous velocity fields obtained from PIV measurements. It shows that most of the low and medium frequency unsteadiness can be accurately describe with a small number of modes. These subset of modes define an efficient filter to analyze these unsteadiness and could be used to rebuild time resolved filtered velocity fields using Linear Stochastic Estimation methods.

Acknowledgments

This work received financial support from the CNES through the research program ATAC as well as from the Labex Mécanique Et Complexité. These supports are gratefully acknowledged.

REFERENCES

Agostini, L., Larchevêque, L. & Dupont, P. 2015 Mechanism of shock unsteadiness in separated shock/boundary-layer interactions. *Physics of Fluids* **27** (12), 126103.

Beresh, S. J., Kearney, S. P., Wagner, J. L., Guildenbecher, D. R., Henfling, J. F., Spillers, R. W., Pruett, B. O. M., Jiang, N., Slipchenko, M. N., Mance, J. & Roy, S. 2015 Pulse-burst piv in a high-speed wind tunnel. In *AIAA Paper 2015-1218, 53rd AIAA Aerospace Science Meeting, Kissimmee, Florida, 5-9 January*.

Beresh, Steven J., Wagner, Justin L., DeMauro, Edward P., Henfling, John F., Spillers, Russell W. & Farias, Paul A. 2016 Applications of temporal supersampling in pulse-burst piv. In *18th International Symposium on the Application of Laser and Imaging Techniques to Fluid MechanicsLISBON — PORTUGAL JULY 4 – 7*.

Dolling, D. S. 2001 Fifty years of shock-wave/boundary-layer interaction research: what next. *AIAA Journal* **39** (8), 1517–1531.

Dupont, P., Haddad, C. & Debiève, J. F. 2006 Space and time organization in a shock induced boundary layer. *Journal of Fluid Mechanics* **559**, 255–277.

Ganapathisubramani, B., Clemens, N. T. & Dolling, D. S. 2009 Low–frequency dynamics of shock–induced separation in a compression ramp interaction. *Journal of Fluid Mechanics* **636**, 397–425.

Jiang, Tetyana, Schreyer, Anne-Marie, Larchevêque, Lionel, Piponniau, Sébastien & Pierre, Dupont 2016 Velocity spectrum estimation in shock-boundary layer interaction. In *AIAA SciTech*, pp. –. American Institute of Aeronautics and Astronautics.

Piponniau, S., Collin, E., Dupont, P. & Debiève, J.F. 2012 Reconstruction of velocity fields from wall pressure measurements in a shock wave/turbulent boundary layer interaction. *International Journal of Heat and Fluid Flow* **35** (0), 176–186.

Piponniau, S., Dussauge, J. P., Debiève, J. F. & Dupont, P. 2009 A simple model for low-frequency unsteadiness in shock-induced separation. *Journal of Fluid Mechanics* **629**, 87–108.

Scarano, F. & Moore, P. 2012 An advection-based model to increase the temporal resolution of piv time series. *Experiments in Fluids* **52** (4), 919–933.

Schreyer, A.M., Larchevêque, L. & Dupont, P. 2015*a* Method for spectra estimation from high-speed experimental data at discrete points in time. In *53rd AIAA Aerospace Sciences Meeting, Kissimmee, Fl, 5-9 January*.

Schreyer, Anne-Marie, Lasserre, Jean J. & Dupont, Pierre 2015*b* Development of a dual-piv system for high-speed flow applications. *Experiments in Fluids* **56** (10), 1–12.

Sirovich, L. 1987 Turbulence and the dynamics of coherent structures. *Quarterly of Applied Mathematics* **XLV**, 561–571.

Wu, M. & Martin, M. P. 2008 Analysis of shock motion in shockwave and turbulent boundary layer interaction using direct numerical simulation data. *Journal of Fluid Mechanics* **594**, 71–83.